IEEE Open Journal of Nanotechnology

Received 10 March 2023; revised 30 May 2023; accepted 5 June 2023. Date of publication 8 June 2023; date of current version 22 June 2023. The review of this article was arranged by Associate Editor John Yeow.

*Digital Object Identifier 10.1109/OJNANO.2023.3284201*

# Tailoring by AgNPs of the Energetics of Charge Carriers in Electrically Insulating Polymers at the Electrode/Dielectric Contact

**KREMENA MAKASHEVA (Member, IEEE), CHRISTINA VILLENEUVE-FAURE (Member, IEEE), ADRIANA SCARANGELLA, LUCA MONTANARI, LAURENT BOUDOU, AND GILBERT TEYSSEDRE (Senior Member, IEEE)**

Laboratoire Plasma et Conversion d'Energie (LAPLACE), Université de Toulouse, CNRS, UPS, INPT, F-31062 Toulouse Cedex 9, France

CORRESPONDING AUTHORS: KREMENA MAKASHEVA; GILBERT TEYSSEDRE (e-mail: kremena.makasheva@laplace.univ-tlse.fr; gilbert.teyssedre@laplace.univ-tlse.fr)

This work was supported in part by l'Agence Nationale de la Recherche in France, Project ANR InTail under Grant ANR-AA-PBLI-II-2011), in part by project IDEX SEPHIR through IDEX ATS 2015 of Université de Toulouse under Grant 2016-066-CIF-D-DRVD, and in part by Project ANR BENDIS under Grant ANR-21-CE09-0008.

**ABSTRACT** The ever increasing field of application of nanodielectrics in electrical insulations calls for description of the mechanisms underlying the performance of these systems and for identification of the signs exposing their aging under high electric fields. Such approach is of particular interest to electrically insulating polymers because their chemical defects are of deleterious nature for their electrical properties and can largely degrade their performance at high electric fields. Although these defects usually leave spectroscopic signatures in terms of characteristic luminescence peaks, it is nontrivial to assign, in an unambiguous way, the identified peaks to specific chemical groups or defects because of the low intensity of the signal with the main reason being that the insulating polymers are weakly emitting materials under electric field. In this work, we go beyond the conventional electroluminescence technique to record spectroscopic features of insulating polymers. By introducing a single plane of silver nanoparticles (AgNPs) at the near-surface of thin polypropylene films, the electroluminescent signal is strongly enhanced by surface plasmons processes. The presence of AgNPs leads not only to a much higher electroluminescence intensity but also to a strong decrease of the electric field threshold for detection of light emission and to a phase-stabilization of the recorded spectra, thus improving the assignment of the characteristic luminescence peaks. Besides, the performed analyses bring evidence on the capability of AgNPs to trap and eject charges, and on the possibility to adjust the energetics of charge carriers in electrically insulating polymers at the electrode/dielectric contact via AgNPs.

**INDEX TERMS** AgNPs, charge trapping, electroluminescence, nanostructured dielectrics, plasma processes, tailored interfaces.

## I. INTRODUCTION

The current trends of constantly increasing energy consumption and the constant demand for ever higher energy density in electrical devices require in many cases a revision of the well-established concepts for detection and control of the processes of charge injection and transport in dielectric materials, and particularly those occurring in electrically insulating synthetic polymers. The electrically insulating synthetic polymers represent a class of polymeric materials, largely used in power electronics and electrical engineering applications, among others high voltage direct current (HVDC) cables for energy transmission lines, generators, transformers, capacitors [1]. These are often polyolefins (polyethylene, polypropylene, etc.) containing some additives. They ensure the performance

of electrical systems but their service life-time is limited by the stresses (electrical, mechanical, thermal, environmental, etc.) they undergo. One should recall here that the insulating polymers are required to sustain very high electric fields over a long time. For example, the typical service field for HVDC cables is in the order of 20 kV/mm and it is one order higher in power capacitors [2]. Such high electric fields undoubtedly cause dynamic processes in the insulating materials, in particular at the electrode(metal)/dielectric contacts. Moreover, additional operations, like abrupt increase/decrease of the electric field, polarity reversal, *etc.*, strongly enhance the electrical constraints. Thus, the reliability of insulating polymers is of paramount importance for the safety operation of the electrical devices. Knowledge on their response to the applied electrical stress is essential in order to determine their safety limits.

## II. ENERGETIC CARRIERS AND ELECTRICAL AGEING

The ability of insulating polymers to sustain high electric fields decreases with time. This deterioration of the electrical strength properties is mainly due to a gradual degradation of the material and often leads to an electrical breakdown, which actually represents the final stage of polymer degradation by electric field. In all cases the degradation process takes certain time and is accompanied by modifications of the response of the insulating polymers to the applied electrical stress. Moreover, according to the conditions and the environmental factors (humidity, oxygen, radiation, corrosive agents, *etc.*) the appearing pre-breakdown patterns may differ. Electrical degradation and aging of insulating polymers represent therefore, a constant research interest in order to understand the fundamental mechanisms behind these effects and to contribute to the design and engineering of highly-performant electrical systems.

The electrical degradation and aging of insulating polymers result from the induced chemical reactions after interaction of thermal or higher energy charge carriers with the material [3], [4], [5]. It can be partially assigned to three distinct mechanisms: (*i*) space charge build-up that inevitably becomes a factor for controlling the charge transport at high electric fields [6], (*ii*) creation of low-density domains or channels in the bulk by carrier injection from electrical contacts [7] and (*iii*) existence in the material of regions with structural heterogeneity for which the local electric field exceeds the averaged one, i.e., regions with different densities or different levels of disorder, giving rise to significantly different conductivities and, hence to a nonuniform field distribution [8]. Regardless the degree of impact on insulating polymers, all works reporting on the above mechanisms agree on the fact that charge trapping, alongside with recombination of charge carriers, is a likely prelude of the electrical degradation of insulating polymers.

In order to experimentally evaluate the above listed mechanisms and to get inside the associated elementary processes, one should rely on both:

1) diagnostic methods revealing information on the charges injection and transport processes at nanoscale. In the last decade, electrical modes derived from Atomic Force Microscopy (AFM), like Kelvin Probe Force Microscopy (KPFM) [9], [10], [11] and Electrostatic Force Distance Curve (EFDC) [12] largely advanced on the subject. They became indispensable to provide information on the density profiles of injected charges and the dynamics of charge injection, trapping, transport and decay in dielectrics [9], [10], [11], [12], [13], [14], [15], [16], [17]. Additional constraints, like thermal activation of trapped charges can also be accounted for in the analyses of charge transport when applying these methods [17]. Moreover, combining these experimental methods with electrostatic modeling brings the charge analysis to a quantification level, providing for example, extraction of the density of injected charges [9], [11], [16], [17] or evidence on the electrical response of the interphase, a transition region, formed between the dispersed nanoparticles (NPs) and the polymeric host matrix in nanocomposite dielectrics [18];
2) diagnostic methods sensitive to the energetics of charge carriers, like electroluminescence (EL) [19], [20], [21], [22], [23], [24], [25], [26], [27]. EL is the excitation of luminescence as a result of the existence of an applied electric field in the probed material. For a polymeric material the EL emission is a dynamic response of charge transport in it. As demonstrated previously [19], [20], [21], [22], [23], [24], [25], [26], [27], the EL appears very appropriate diagnostic tool to address the electrical aging of insulating polymers because the degradation process involves energy dissipation in the energy range of chemical bonds (of a few eV) that corresponds to the UV-vis range of the optical spectrum. The appearance of EL can be considered as a sign for the beginning of aging of insulating polymers under electrical stress. Spectroscopic analyses thus give indications on the nature of the transition processes, i.e., on the dissociative versus non-dissociative relaxation of excited states, defining in that way the nature of the energy decay mechanism: chemical versus physical one.

Given the covered energy range, the EL of insulating polymers is a specific response of the material that shows charge-structure interactions including relaxation of the kinetic energy of hot carriers, or modifications in their potential energy during radiative recombination of charges [21], [22], [23], [24], [25], [26], [27]. However, one of the major challenges to meet when analyzing the EL spectra from insulating polymers is the low intensity of the recorded signal. This problem becomes even more complex in the case of polyethylene and polypropylene, since these are weakly emitting materials under electrical field [25], [26], [27]. As a result, the low resolution prevents from a fine interpretation of the recorded spectra. To overcome this issue, we have developed a methodology for analysis of the spectroscopic signature of insulating polypropylene films based on alteration of the energetics of

charge carriers at the electrode/dielectric contact by silver nanoparticles (AgNPs)-tailoring. This approach leads to a strong enhancement of the intensity of the characteristic EL spectra.

## III. RATIONALE OF INTRODUCING SILVER NANOPARTICLES AS ARTIFICIAL DEEP TRAPS AT THE ELECTRODE/DIELECTRIC CONTACT

As mentioned earlier, the electrical aging of insulating polymers finds its origin in several mechanisms; one of which is injection of charge carriers (negative and positive, depending on the applied polarity) at the electrode(metal)/dielectric contact. Accumulation of electric charges in the polymer bulk leads to the formation of internal space charge [28], [29]. The latter modifies the design electric field creating a much different internal electric field distribution that can trigger local damages in the structure and thus, lead ultimately to breakdown [6], [30]. In the last two decades a solution to this problem is pursued in the fabrication of nanocomposite dielectric materials or the so-called nanodielectrics. Nanodielectrics, as firstly reported by Lewis in 1994 [31], represent a promising way to increase the performances and improve the reliability of electrical insulations [32]. Not only the resistance to discharge, a well-known property improvement with the incorporation of inorganic particles into insulating synthetic polymers, but also the dielectric strength and volume resistivity have been reported enhanced when dealing with nanocomposites with well dispersed NPs [33]. The space charge behavior can be improved too; dispersion of NPs in the insulating polymer appears fairly efficient in suppressing space charge build-up [34], [35]. However, the major difficulty in the process is dispersion of the NPs. It appears quite challenging and often leads to formation of large aggregates of the NPs that prevent from achieving the desired effect. An alternative to this way is an action of the NPs at the level of the dielectric interfaces, i.e., at the macroscale interfaces. If the NPs are capable to efficiently stabilize charges, i.e., being artificial deep traps for charge carriers, the resultant field at the metal/dielectric interface would be reduced and thus the injection self-limited. Recently, this approach has been successfully demonstrated. The creation of artificial deep traps with metallic (silver) nanoparticles embedded in a plasma processed thin insulating layer constitutes an efficient way for mitigation of space charge build-up in low density polyethylene (LDPE) [36]. The AgNPs form deep traps at the interface in such a way that the injected charges are permanently trapped. This entails two effects: (*i*) the trapped charges induce a counter field to moderate the injecting field at the electrode/dielectric contact thereby reducing further injection and (*ii*) the already trapped charges are not available for transport anymore. A rough estimation based on the Poisson's equation shows that, in order to reduce an electric field of, for example, 10 kV/mm at the electrode/dielectric contact, a trap surface density of $6 \times 10^{11}$ cm$^{-2}$ is needed. Such trap density represents an inter-particle distance of 13 nm if each particle holds one charge only. In order to do so, we have processed a single layer of AgNPs covered by a very thin organosilicon layer [36]. By their metallic nature, the AgNPs stabilize the injected charges and the thickness of the organosilicon layer covering the AgNPs allows transport of the injected charges to the AgNPs for an efficient capture.

Another advantage of this concept resides in modification of the energetic levels at the electrode/dielectric interface that would turn in a change of the charge injection efficiency. Generally, the charge injection in insulating materials cannot be a feature of charges passing over the energetic barrier from the metal into a perfect wide band gap material (dielectric). The energetic barrier for this process is reported to be of around 4 eV in polyethylene, which would make the injection highly improbable, since requiring highly energetic charge carriers [4]. With such a high value of the energetic barrier, the theoretically predicted injection current, as derived from the classical injection laws of Schottky and Fowler-Nordheim, should remain virtually zero for electric field strengths and temperatures for which the injected charges and current are experimentally detected in insulating polymers. Both experimental and modelling works point to a much lower injection barrier, of around 1 eV, called apparent injection barrier [4]. Besides, modelling of the charge transport in polyethylene under nonstationary conditions indicates that the trapping sites follow an exponential distribution from the energy band edges into the gap [37], [38]. Such description is consistent with the existence of chemical traps (forming the deepest levels) and physical traps (forming the shallowest levels). Our interest here is mostly directed to the chemical traps, as representative of deep traps, for the following reasons:

1) The chemical traps (defects) are of deleterious nature for the electrical properties of insulating polymers and can largely degrade their performance;
2) Through their density, the deep traps govern the tail of the trap distribution;
3) The early stage of electrical degradation would be the formation of chemical defects that are potentially also deep traps as viewed from the energy band structure.

The chemical defects in insulating polymers usually leave spectroscopic signatures in terms of characteristic luminescence peaks. Yet, it is nontrivial to assign these peaks to specific groups of defects in an unambiguous way due to the low intensity of the recorded signal, besides the lack of exhaustive database for optical signatures of chemical defects. One shall recall here that the insulating polymeric materials are not supposed to emit light. It presumes that their EL-spectra can directly be related to the energy exchange with existing defects and to the possible modifications of their structure under applied electric stress. Insertion of a single layer of AgNPs (artificial deep traps) at the electrode/dielectric contact would allow, depending on the size, shape and density of the AgNPs, to alter the energetics of charges carriers to be injected and therefore, to activate the chemical traps, and to probe the different transition processes in the insulating polymeric material. This represents the working hypothesis of our study.

**TABLE 1. Summary of the Main Characteristics of the Studied Nanostructures**

| | Parameters for the Ag-sputtering in Ar-plasma | | | | Silver nanoparticles – AgNPs | | | | | Energy band gap of the AgNPs/BOPP nanostructure (eV) [b] | SiOC:H cover layer thickness (nm) [c] |
|---|---|---|---|---|---|---|---|---|---|---|---|
| | Power (W) | $V_{dc}$ (V) | pressure (Pa) | time (s) | | Size (nm) | Surface density ($NPs/cm^2$) | LSPR energy (eV) | Work function (eV) [a] | | |
| BOPP | 20 | -546 | 5.4 | 5 | Small | < 7.0 | -- | 2.82 | 4.79 | 5.87 | -- |
| | 40 | -750 | 5.4 | 5 | Medium | 11.3 ± 2.4 | $3.6 \times 10^{11}$ | 2.72 | 4.74 | 5.80 | -- |
| | 80 | -1000 | 5.4 | 5 | Large | 19.7 ± 4.8 | $1.3 \times 10^{11}$ | 2.46 | 4.69 | 5.75 | 6.5 ± 0.2 |
| | 80 | -1000 | 5.4 | 12 | Percolated layer | | | -- | -- | -- | -- |
| $SiO_2$/Si | 80 | -1000 | 5.4 | 5 | Large | 19.6 ± 4.4 | $1.7 \times 10^{11}$ | -- | 4.70 | -- | 24.2 ± 0.6 |

[a] The work function of pure silver is 4.64 eV [40].
[b] The energy band gap of BOPP is 7.0 eV [43]
[c] The SiOC:H cover layer was deposited only on the entire structures.

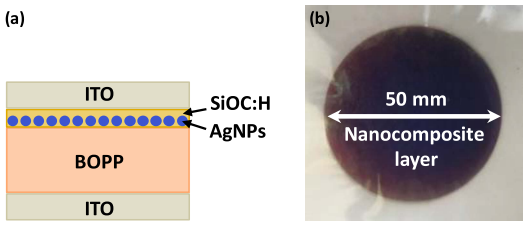


**FIGURE 1. (a) Schematic of the AgNPs-based nanostructure in cross-section view and (b) optical image of the final sample taken on the top.**

## IV. EXPERIMENTAL DETAILS

### A. DESCRIPTION OF THE STRUCTURES AND THE PLASMA PROCESS

The insulating polymer material under study was a thin bi-oriented polypropylene (BOPP) film (thickness of 17.8 μm). The BOPP film, provided by KOPAFILM, Germany, was with different roughness for the two faces.

A thin nanocomposite layer, consisting of a single plane of AgNPs covered by a very thin (∼5 nm) organosilicon (SiOC:H) layer, was deposited on the face of larger roughness of the BOPP film by a plasma process [36], [39]. To perform the EL-measurements the AgNPs/SiOC:H-tailored BOPP sample was both sides covered by 130 nm-thick ITO layers with 90% transparency and resistivity of $16 \times 10^{-3}$ Ω/sq. The electrode diameter was 50 mm. A schematic cross-view of the structure is shown in Fig. 1(a) and an optical image on top of the final AgNPs/SiOC:H-tailored sample is given on Fig. 1(b). In addition, the same AgNPs/SiOC:H stack was deposited on 520 nm-thick $SiO_2$ layers, thermally grown on Si-substrates for the KPFM analysis of charge injection at nanoscale.

The plasma deposition of the AgNPs/SiOC:H stack was performed in two-steps: 1) silver sputtering to obtain the single plane of AgNPs followed by 2) plasma polymerization to create the organosilicon (dielectric) cover layer. For both steps we have used an axially-asymmetric RF (13.56 MHz) capacitively-coupled discharge maintained at low gas pressure that successfully combines sputtering of a metal target and plasma polymerization. Details about the plasma process are given elsewhere [36], [39].

The presented in this work AgNPs were formed by sputtering of a silver target (Inland Europe, with purity of 99.99%) in a pure argon plasma maintained at low gas pressure of p = 5.4 Pa. For the analysis in this work the work function of pure silver is taken $\Phi_{Ag} = 4.64$ eV [40]. The injected RF power in the plasma was of P = 20, 40 and 80 W that induced self-bias voltages of $V_{dc} = -546$, $-750$ and $-1000$ V, respectively on the powered electrode (the silver target) to perform the sputtering. The sputtering time was fixed to 5 s or to 12 s. The parameters characterizing the AgNPs, and those for the entire nanostructures, are summarized in Table 1. For clarity of the presentation, Table 1 also contains results for the energy band gap of the nanostructures and the work function of the AgNPs, as obtained in this work, Section V-B and V-C, respectively.

The organosilicon dielectric cover layer was obtained in the same reactor in the plasma of argon (Air Liquid ALPHAGAZ 2 with a purity of 99.9995%)-hexamethyldisiloxane (HMDSO, $C_6H_{18}OSi_2$, Sigma-Aldrich with a purity >99.5%) mixture maintained with power of P = 80 W ($V_{dc} = -900$ V) at total pressure of $p_{tot} = 6.6$ Pa. The thickness of the SiOC:H cover layer was controlled by the deposition time.

### B. STRUCTURAL AND OPTICAL CHARACTERIZATION OF THE SAMPLES

At each step of the elaboration process the samples were structurally and optically characterized. The size and surface density of AgNPs were determined after processing of Scanning Electron Microscopy (SEM) images taken with a JEOL JSM 7800F microscope. Optical transmittance spectra were recorded using a Hewlett Packard HP8452A Diode Array Spectrophotometer in the UV–vis–NIR range (190 – 820 nm) to obtain the position of the AgNPs Local Surface Plasmon Resonance (LSPR) and to deduce the energy band gap. A

Semilab 2000 spectroscopic ellipsometer was used in the 250 – 850 nm spectral range with an incident angle of 75° to determine the thickness and the optical properties of the organosilicon cover layers. Forouhi-Bloomer dispersion law was applied to proceed the recorded ellipsometric spectra. AFM topography analysis of the sample surfaces was performed in tapping mode with a Bruker Multimode 8 set-up using a TESPA-V2 probe.

### C. ELECTRICAL CHARACTERIZATION OF THE SAMPLES

KPFM in Amplitude Modulation mode (AM-KPFM) was applied to bring evidence on the trapping capabilities of the AgNPs and characterize the charge injection and decay mechanisms at nanoscale. The same, as for the AFM topography, Bruker Multimode 8 set-up was used. A specific methodology, presented elsewhere, was employed to ensure results accuracy and reproducibility [10]. A PtIr-coated Si-tip (curvature radius $R_c = 25$ nm) was used to inject charges and to probe the resulting surface potential modifications. The experiments were performed under $N_2$ atmosphere. Charges were injected in contact mode (contact force 20 nN) after applying a bias from -10 V to +25 V with a step of 5 V during 1 min. Surface potential at the charge injection zone was probed with the same AFM-tip at a lift of 5 nm.

EL measurements [23], [26], [27] were achieved under secondary vacuum ($<10^{-4}$ Pa) in order to avoid electrical discharges in the ambient. They were performed under AC voltage with frequency of 50 Hz and electric field, up to 180 kV/mm as crest value, using a voltage amplifier (Trek 20/20c). Luminescence was recorded using cooled detectors; the latter being a photomultiplier (Hamamatsu R943-02) in photon counting mode for EL-field intensity and phase patterns measurements, and a CCD camera (LN /CCD-1100-PB from Princeton Instruments) coupled to a grating dispersive system (Jobin-Yvon CP200) for spectra acquisition. With using 1 mm-width slits at the entrance and exit of the dispersive system, the spectral resolution of the whole detection chain was about 4.5 nm. For these EL experiments, the periphery of the 50 mm-diameter ITO electrodes was covered with a silicone rubber ring in order to avoid edge effects in the emission [27]. Light emitted from the central part (20 mm in diameter) of the top ring electrode was detected and analyzed.

### D. COMPUTATIONAL APPROACH

Better understanding of the charging mechanisms was achieved after modelling some of the aspects of the studied structures. A simple 2D-axisymmetric electrostatic model of the structures based on Finite Element Model (FEM) and developed earlier on COMSOL Multiphysics was applied [17]. The model geometry considered the dielectric $SiO_2$ sample, the AgNPs/SiOC:H nanocomposite and the AFM tip. The surrounding air box was selected with large enough dimensions to avoid edge effects. The AFM tip was represented as a 10 µm-height truncated cone (10 µm-height and 14° of aperture angle) ending with a semi-spherical apex (curvature radius $R_c = 25$ nm, the same as the one used in the experiment). The AgNPs/SiOC:H-tailored BOPP samples, as applied in the EL-measurements were represented by a Metal-Insulator-Metal (MIM) structure. For both configurations the Poisson's equation was solved in the air and in the dielectric structure to determine the electric field distribution. The sample surface (for the AFM-case) and the dielectric parts (AgNPs/SiOC:H stack, $SiO_2$ and BOPP) were considered free of charges. The dielectric permittivity of different dielectric parts considered in the model were taken as measured at low frequency (1 kHz): $SiO_2$ ($\varepsilon_r = 3.9$, [41]), SiOC:H ($\varepsilon_r = 3.0$, [42]) and BOPP ($\varepsilon_r = 2.25$, [43]). More details on the model and different geometrical configurations are given elsewhere [17].

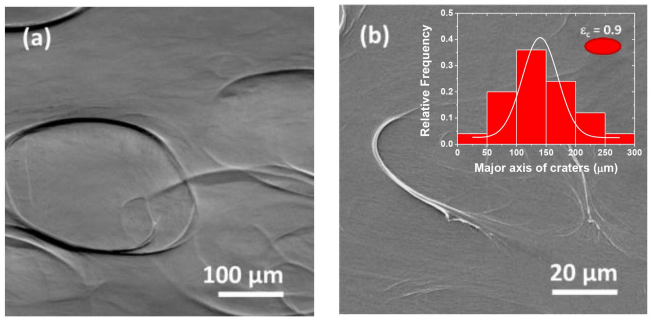


**FIGURE 2.** SEM images of bare BOPP (rough face): (a) Sample tilted at 15° degrees. Image underlying the embedded in each other crater-like patterns and (b) top view of the crater-like patterns, in inset: Statistics performed on over 50 crater-like patterns (bin sizes, Gaussian distribution function and example of a shape with high eccentricity level).

## V. RESULTS AND DISCUSSION

### A. MORPHOLOGICAL ANALYSIS OF BARE BOPP AND AGNPS-TAILORED BOPP AND $SIO_2$ SAMPLES

Since the studied insulating BOPP films present an important roughness on both faces, and specifically on the face that is intended to be tailored by AgNPs we have performed a morphological surface analysis based on SEM observation and AFM measurements. Fig. 2 shows large scale images of the rough face of bare BOPP. One can clearly notice on Fig. 2(a) crater-like patterns that are embedded in each other. The craters were formed during the BOPP film fabrication with as purpose to favor oil impregnation in capacitor manufacturing [44]. The craters are randomly distributed in the plane of the BOPP film. They have elliptical shape with parallel oriented major axis (Fig. 2(a)) varying between 40 and 300 $\mu$m, with average size of 141.3 $\pm$ 56.3 $\mu$m and highly expressed eccentricity level, comprised in the range $0.75 < \varepsilon_c < 0.95$. The inset of Fig. 2(b) shows details on the statistics performed on over 50 crater-like patterns. The distribution in size of the major axis of the craters follows a Gaussian distribution, which confirms the random feature in their appearance. Elliptical shape with eccentricity of $\varepsilon_c = 0.9$ is given as an example of the most frequently observed one.

High resolution SEM observations of bare BOPP films were performed inside and outside the craters, pointing out

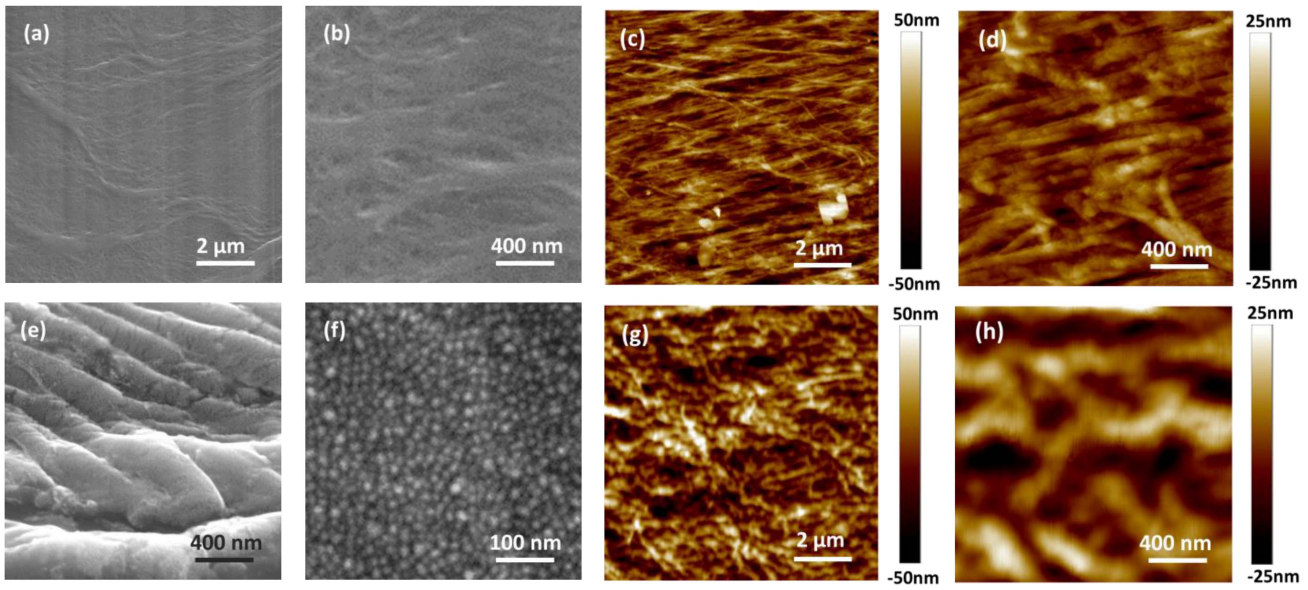


**FIGURE 3.** SEM and AFM images: (a)–(d) Bare BOPP and (e)–(h) AgNPs-tailored BOPP film. AgNPs were produced for $t_s = 5$ s in the plasma sustained with power P = 80 W ($V_{dc} = -1000$ V), at pressure p = 5.4 Pa. All SEM images represent top views of the samples, except image (e), for which the sample was tilted at 15°.

to the same results. Looking on the images (Fig. 3(a) and (b)) one can clearly identify the fibrous structure of the BOPP film. The fibers are less than 100 nm thick and the cavities between the fibers can attain 100 nm width at some places. AFM topography measurements (Fig. 3(c) and (d)) confirm the fibrous nature of the BOPP film. They even go further, suggesting that the cavities between the fibers are of at least 50 nm depth (Fig. 3(c)). The fibrillated structure observed here is the consequence of the destruction of the spherolitic structure upon drawing [45]. Polymorphism, orientation and morphology deeply impact physical properties of PP, including the electrical conductivity [46].

The effect of AgNPs on the BOPP samples is presented in Fig. 3(e)–(h). These AgNPs were synthesized with plasma power of 80 W for sputtering time of 5 s, and are called hereafter "large" AgNPs. There is no evidence of conformational changes in the polymer structure when tailoring the rough face of the BOPP with AgNPs. The AgNPs monolayer is conformal to the BOPP surface, which can be clearly seen in the SEM image taken on the 15°-tilted sample on Fig. 3(e). The AgNPs follow the BOPP fibers and spread in between them, in the cavities. The monolayer of AgNPs covers the entire surface, despite the presence of crater-like patterns on the BOPP surface. This is due to the fact that the waviness imposed by the craters is not abrupt enough to prevent from plasma deposition on the slopes of the crater-edges. Image processing of Fig. 3(f) shows that the reported in Fig. 3 AgNPs are of mean size of 19.7 ± 4.8 nm, assuming sphericity of the nanoparticles (statistics made on over 300 nanoparticles). They are homogeneously distributed in the plane and their surface density is $1.3 \times 10^{11}$ NPs/cm$^2$. Differential analysis of the AFM topography (Fig. 3(c) and (g)) points out to a

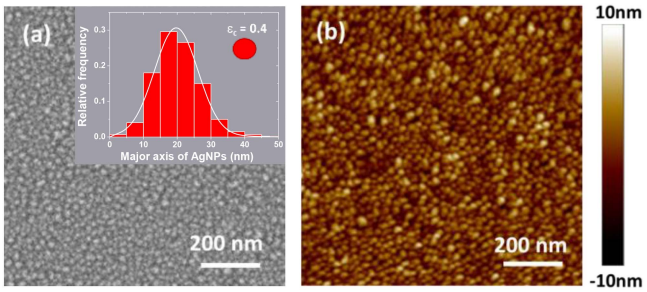


**FIGURE 4.** (a) SEM top view image of AgNPs single layer deposited on $SiO_2$ surface (plasma parameters: P = 80 W ($V_{dc} = -1000$ V), p = 5.4 Pa, $t_s = 5$ s). Inset: Histogram of the AgNPs sizes with statistics on over 500 AgNPs and an example of low eccentricity level, observed in the AgNPs-shape; (b) AFM topography of the same sample.

conservation of the cavity depths in the BOPP fiber organization in presence of AgNPs. AFM topography performed on the AgNPs-tailored BOPP at higher resolution (Fig. 3(h)) confirms the waviness of the surface revealed by the SEM observations (Fig. 3(e)).

Morphological analysis of the AgNPs-tailored $SiO_2$ sample (Fig. 4) does not show any significant difference when compared to the AgNPs-tailored BOPP one. A reason might be the non-polar character expressed by both surfaces, the $SiO_2$ and the BOPP. The AgNPs deposited on the $SiO_2$ sample are of mean size of 19.6 ± 4.4 nm with a surface density of $1.7 \times 10^{11}$ NPs/cm$^2$, as extracted from the SEM image (Fig. 4(a)). The histogram, presenting the relative frequency in each bin size shows Gaussian distribution in size of the AgNPs. Their shape is ellipsoidal (of prolate spheroid type), with relatively low level of eccentricity, $\varepsilon_c < 0.4$. The average

edge-to-edge distance between two large AgNPs in the plane is found of 5.2 ± 3.5 nm after processing of the SEM images.

Combined SEM-analysis and AFM-morphology measurements (Fig. 4(b)) allow to confirm that the shape of the AgNPs is of prolate spheroid, as obtained in our previous studies for the same family of samples [39], [47]. The obtained upper limit of the eccentricity level of $\varepsilon_c = 0.4$ means that the minor axis of the AgNPs is of only 8% smaller than the major one. This finding suggests that for further analyses the AgNPs can be considered spherical ones and supports the sphericity approximation made earlier for the statistical analysis of AgNPs deposited on BOPP.

In addition to the presented on Figs. 3 and 4 samples for large AgNPs (plasma power of 80 W), we have studied BOPP and $SiO_2$ samples tailored with smaller size AgNPs, corresponding to lower values of the applied power to sustain the plasma at the same argon pressure and for the same sputtering time (Table I). When reducing the plasma power, the mean size of the resulting AgNPs gets smaller. It is of 11.3 ± 2.4 nm for 40 W (called "medium" AgNPs) and less than 7 nm for applied power of 20 W (called "small" AgNPs). In contrary, the surface density of the AgNPs increases. An increase with a factor of 2 of the surface density of AgNPs is observed when the applied power to sustain the plasma is halved. The size and surface density of AgNPs are also dependent on the sputtering time. For short sputtering times ($t_s$ = 5 s), at fixed applied plasma power and pressure, the single plane of AgNPs is sustained of discrete AgNPs while for longer sputtering times ($t_s$ =12 s) the AgNPs are percolated, forming a continuous metallic layer.

The organosilicon layer that covers the AgNPs and also spreads in between them is conformal to the nanoparticles. It is of dielectric nature and has multiple functions: 1) it prevents from fast oxidation of the AgNPs, 2) it avoids agglomeration of the AgNPs and 3) it separates, physically and electrically, the AgNPs from the electrode, thus preventing from leakage current. The SiOC:H layer thickness is controlled by the deposition time. For the EL-experiments the SiOC:H layer covering the AgNPs was only 6.5 ± 0.2 nm thick, as measured by spectroscopic ellipsometry. The AM-KPFM measurements were performed on samples with a thicker SiOC:H layer (thickness of 24.2 ± 0.6 nm) aiming at to better explore the charge injection mechanisms.

### B. EVIDENCE OF AGNPS LOCALIZED SURFACE PLASMON RESONANCE IN THE BOPP SAMPLES

Knowledge of the optical properties of the elaborated nanocomposites is essential for the analyses of EL-spectra below because, as it is well-known, owing to their reduced size the AgNPs allow energy concentration at a scale drastically smaller than the corresponding wavelength of the probing light, thus supporting LSPR [48]. The AgNPs, among other metallic nanoparticles such as gold and copper, actually realize the best nanoscale antennae in the visible range of the spectrum. UV-vis-NIR transmittance spectra of the elaborated nanocomposite samples containing AgNPs are presented in

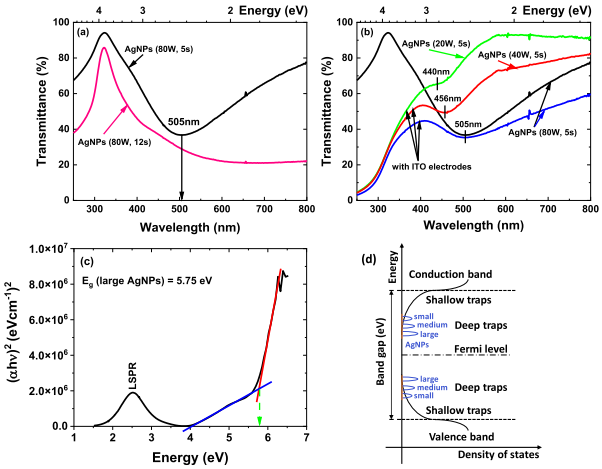


**FIGURE 5. (a) Transmittance spectra of the BOPP structures with AgNPs elaborated for different sputtering times. Comparison between discrete (P = 80 W, $t_s$ = 5 s) and percolated (P = 80 W, $t_s$ = 12 s) AgNPs in terms of presence of LSPR of AgNPs; (b) Influence of the AgNPs size and ITO layers on the transmittance spectra; (c) Tauc's plot for the AgNPs/BOPP stack and (d) schematic of an energy diagram presenting the artificial deep traps induced by the AgNPs.**

Fig. 5. Fig. 5(a) shows spectra for a monolayer of discrete large AgNPs, the same as given in Fig. 3, and for a monolayer of percolated AgNPs. The transparency of this AgNPs/BOPP stack is preserved in the entire energy range, although a strong absorption is observed at 505 nm (2.46 eV), which denotes the LSPR of the discrete large AgNPs. As expected, the LSPR disappears when the AgNPs are percolated in the layer. Such behavior is well-known from the literature of plasmonic studies. It is now established that the LSPR depends on the morphology, composition, and local environment of the nano-inclusions [49]. For comparison, the theoretical LSPR of the same large and discrete AgNPs but embedded in a $SiO_2$ host matrix points to 419 nm (2.96 eV) and the experimental one was found at 456 nm (2.72 eV) [50]. The obtained red shift of the LSPR of the AgNPs here is mainly due to their environment i.e., the BOPP polymer which is in contact with the AgNPs, as well as to deviation in their morphology (shape, eccentricity, *etc.*) and their distribution in size.

As discussed above, when the AgNPs are elaborated with lower plasma power they are smaller in size. A size-decrease of the AgNPs results in a blue shift of their LSPR (Fig. 5(b)). Compared to the one of large AgNPs the LSPR of medium AgNPs is found at 456 nm (2.72 eV) and the one of small AgNPs appears at 440 nm (2.82 eV). The influence of the conductive ITO electrodes is also given in Fig. 5(b). One can notice that the conductive ITO electrodes limit the optical analyses to the near UV – visible range of the spectrum only (>320 nm), which nonetheless remains in accordance with the targeted energies for the study of electroluminescence spectra of BOPP films. Speaking in terms of energy barrier for charge injection, the variation in size and density of the AgNPs at the electrode/dielectric interface is expected to result in a stronger energy confinement for the smaller AgNPs.

Analysis of the energy band gap of the AgNPs-tailored BOPP samples was performed according to the Tauc's law. However, to account for the nanostructured nature of the studied samples we convert this heterogeneous system in a homogeneous effective medium following the effective media approximation (EMA) rules. In general, nanostructured materials can be considered as a mixture of individual components each of them possessing their own continuum-like optical response. Treating a nanostructured material as a mixture having continuum behavior offers the possibility to find the macroscopic (averaged) field quantities by using an approximate treatment [51], [52]. Thus, the energy band gap of each sample was extracted after transformation of the recorded transmittance spectrum to the corresponding absorbance one and deduction of the energy dependent absorption coefficient. It was considered that the energy band gap is direct for the studied here nanocomposites. Following the Tauc's approach a linear fit of the fundamental peak was applied to the absorption plot. In order to account for the mixed nature of the samples, a second linear fit was applied to the slope below the fundamental absorption, thus correcting for the baseline, as described in the work of P. Makuła et al., [53]. The intersection point of the two fitting lines gives the energy band gap (Fig. 5(c)). The LSPR is also clearly indicated on the Tauc's plot, pining the energy absorption of the AgNPs. Following this methodology, the energy band gap was deduced for each of the studied nanostructures (Table 1). The thus obtained energy band gap was smaller (below 6.0 eV) than the one of bare BOPP ($E_g = 7.0$ eV) [43]. It suggests that the AgNPs, as metallic inclusions, create traps into the BOPP energy band gap, placed deeply in the exponential trap distribution (Fig. 5(d)). As discussed in Section III, the deep charge traps in insulating polymers are usually considered of chemical nature and typically associated with chemical additive and defects. Introduction of artificial deep traps, via the AgNPs, at the electrode/dielectric interface conveys a very interesting feature to the BOPP film. Upon excitation, the AgNPs would concentrate energy enough to highlight the chemical groups involved in the electrical degradation process. Moreover, the metallic nature of the AgNPs would most likely prevent from possible chemical interactions with the probed chemical groups. However, polarization effects due to the LSPR of the AgNPs and their interaction with the BOPP film are likely. They could induce modifications in the apparent energy depth of the created traps.

As expected, the energy band gap of the nanostructures increases with decreasing the size of AgNPs from $E_g = 5.75$ eV for the nanocomposites containing large AgNPs to $E_g = 5.80$ eV for the medium AgNPs, to finally get to $E_g = 5.87$ eV for the small AgNPs (Table 1). It means that larger in size AgNPs create deeper in energy trap levels. According to the size of the AgNPs, these artificial traps will require an escape energy of $E_{trap} = 0.63$, 0.60 and 0.57 eV for the large, medium and small AgNPs, respectively (Fig. 5(d)). Therefore, depending on their size, the AgNPs will trap the injected from the electrode charge carriers according to the energy of the latter. As a result, varying the AgNPs size and/or morphology would rise possibilities to selectively probe different chemical functions, as well as their transformation in the BOPP film due to electrical degradation, if any.

### C. EVIDENCE OF CHARGE TRAPPING AND EJECTION BY AGNPS

The intensive studies on charge transport in nanostructures containing metallic nanoparticles, embedded or not in dielectric matrices, are stimulated by the latest applications of these assemblies in technologically advanced devices, among others, plasmonic and plasmoelectronics [54], [55], [56], neuromorphic computing [57], [58], catalysis [59], [60]. The reported results show that the AgNPs are of capacity to trap and eject charges and to induce "hot" carriers (electrons and holes), i.e., carriers with energies larger than those of thermal excitations at ambient temperature [61], [62], [63]. For the nanostructures elaborated in this work it is very important to evaluate whether the injected charges from the electrode are trapped by the AgNPs. Such scenario is intuitive but far from obvious one due to the dielectric matrix that separates the AgNPs from the electrode. Therefore, an experimental demonstration of charge trapping by the AgNPs is essential. To that end, AFM in AM-KPFM mode was applied to inject charges in the nanocomposite stack containing a monolayer of large AgNPs, following a methodology developed earlier [10]. After injection of charges at a given bias, applied to the AFM-tip during 1 minute, the surface potential of the charge spot was measured and its profile was extracted, as shown in Fig. 6(a) for a bias of 25 V. The surface potential profile has typical Gaussian shape. Fig. 6(a) compares the surface potential profiles obtained after charge injection in 24.2 nm thick SiOC:H films with or without embedded AgNPs, deposited on a thin $SiO_2$ layer grown on Si-substrate. The measured surface potential profile on the bare SiOC:H layer, via its narrow Full Width at Half Maximum (FWHM, called W hereafter), reflects the fact that the injected charges are trapped in the dielectric, close to the injection point. When the AgNPs are embedded in the SiOC:H layer close to its surface (at 24.2 nm in this case) the obtained results reveal a higher maximum of the measured surface potential, as well as a larger width of its profile (Table 2). In a first approximation (structures with equal total thicknesses) the area under the recorded surface potential profile $I_s$ accounts for the amount of stored charges at the injection point. For the same applied bias and injection time, the difference in the stored charges between the organosilicon and the nanocomposite layers is the part of injected charges that have been trapped by the AgNPs.

The impact of AgNPs on charge injection is confirmed on Fig. 6(b) for various applied injection voltages on the AFM tip for both polarities. It emphasizes an increase of the injected charge density with increasing the applied bias. Indeed, in presence of AgNPs the amount of injected charges is always higher compared to the bare SiOC:H, which implies charge trapping not only in the insulating layer but also by the AgNPs. The impact of organosilicon layer on the amount of

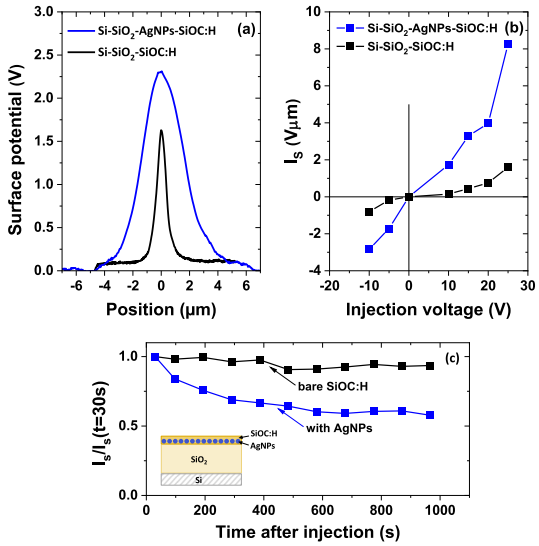


**FIGURE 6.** Trapping capability of AgNPs embedded in organosilicon (SiOC:H) matrix at 24.2 nm beneath the surface (blue curves) compared to the SiOC: H matrix alone (black curves): (a) Cross-section of the potential profiles after charge injection during 1 min at 25 V; (b) integrated potential profiles after 1 min of charge injection as a function of the injection voltage, and (c) decay in time of the integrated potential profile, normalized to its value at 30 s (practical time needed to start measurements), after charge injection during 2 min at 25 V, inset: Sketch of the studied structure.

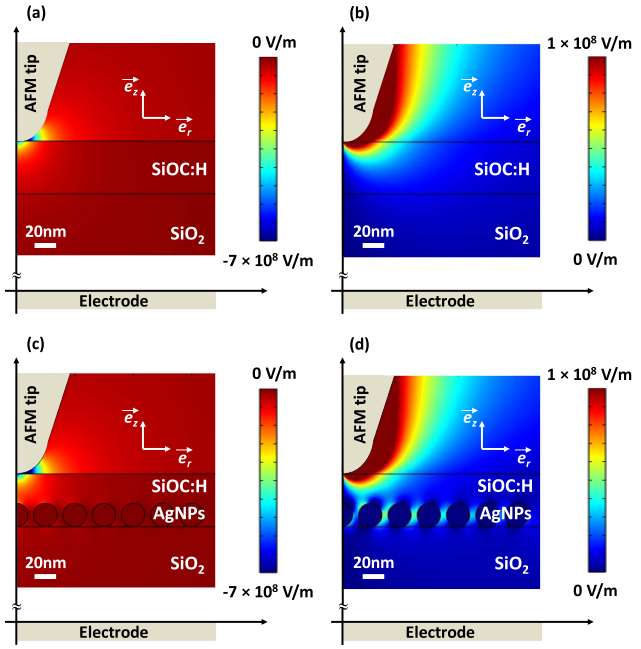


**FIGURE 7.** Spatial distribution of the electric field after electrostatic calculations under AFM configuration: (a), (b) In the organosilicon layer and (c), (d) in the nanocomposite structure. In (a) and (c) axial component of the electric field and in (b) and (d) radial component of the electric field for charging at 10 V applied at the AFM tip.

**TABLE 2.** FEM Model Parameters and Quantity of Trapped Charges

| | $SiOC:H/SiO_2/Si$ stack | SiOC:H with embedded AgNPs on $SiO_2/Si$ stack |
|---|---|---|
| Measured Surface Potential Profiles parameters | | |
| $V_m$ (V) | 1.7 V | 2.4 V |
| W (μm) | 0.5 μm | 2.5 μm |
| FEM model parameters | | |
| $W_r$ (μm) | 0.35 μm | 3.0 μm |
| $W_z$ (nm) | 20.0 nm | 20.0 nm |
| Quantity of Trapped Charges | | |
| Q (C) | $0.12 \times 10^{-16}$ C | $2.0 \times 10^{-16}$ C |

charges injected in the AgNPs is essential due to the intrinsic dielectric charging properties of the SiOC:H matrix. Although remaining a good insulator, the SiOC:H layer is slightly more conductive compared to a $SiO_2$ one, for example. It actually controls the transport of charges injected from the electrode (AFM tip in this case) to the AgNPs. The effect of introduction of AgNPs into a SiOC:H layer is more pronounced compared to a $SiO_2$ layer and the reached maximum of the surface potential is higher under the same injection voltage and time [17], [39].

Furthermore, the embedded AgNPs in the SiOC:H layer accelerate the charge decay before charge stabilization as shown on Fig. 6(c). Whereas for the bare organosilicon layer the charges are trapped in the dielectric close to the injection point and remain trapped over more than 15 min, as expected for a good dielectric (only 6% decrease in time is observed in the measured area of the surface potential profile), the presence of AgNPs induces a quick charge transport from the injection point to the AgNPs before stabilization. The measured area under the surface potential profile of the nanocomposite structure decreases almost twice in a 15 min time after charge injection (decrease of 42%). It means that the injected charges are conducted away from the injection point. Such dynamic response of the system indicates that the injected charges from the AFM tip are transported through the SiOC:H layer, via tunneling, hopping and/or Poole-Frenkel mechanisms of conduction, to reach the monolayer of AgNPs before being laterally spread by tunneling between the AgNPs in the plane and trapped by the AgNPs. The obtained edge-to-edge distance between the AgNPs of around 5 nm supports this assumption.

The above demonstrated charge trapping by the AgNPs is confirmed by calculations of the spatial distribution of the electric field of the structures without and with AgNPs (Fig. 7). As expected from general considerations, under AFM conditions (tip-to-sample geometrical configuration) the electric field is divergent, localized at the AFM tip, and has a maximum at the triple point (electrode-dielectric-air) where it reaches $|E| = 5.8 \times 10^8$ V/m for the sample without AgNPs (Fig. 7(a) and (b)). Its strength straightforwardly determines the amount of injected charges at the contact point, and thus the maximum of the measured surface potential (Fig. 6(a)).

One should recall here that the charge injection and the surface potential probing after injection are performed with the same AFM tip in a two-step protocol [10]. The surface potential profile broadening, and more significantly the variation of the area under the profile, is then defined by the charge transport in the dielectric, both laterally and in depth. As shown in Fig. 6(c) for the bare SiOC:H layer, the area under the surface potential profile varies slightly in time after charge injection. It means that the charges remain trapped in the very small area around the injection point, which in a way confirms the good dielectric nature of the SiOC:H layer.

In presence of AgNPs the situation changes radically. One observes a very strong capacitive coupling between the AFM tip and the AgNPs, mainly those that are located under the AFM tip (Fig. 7(c) and (d)). Like in the case without AgNPs the electric field is maximum under the AFM tip but its strength is higher ($|E| = 6.4 \times 10^8$ V/m). Such electric field strength is high enough to promote charge injection/conduction based on non-linear electric field behavior in the frame of the Poole-Frenkel formalism [64]. The required electric field threshold for switching on the field-dependent charge conductivity is $|E_{th}| = 2.0 \times 10^8$ V/m, as measured for $SiO_2$ thin layers [65]. It suggests that a non-linear behavior in the charge transport should be expected when the AgNPs are embedded in the dielectric layer. Their role in the field amplifications is essential. They adjust the electric field at the electrode/dielectric contact as function of their size and also their distance to the electrode, i.e., the thickness of the SiOC:H cover layer.

The axial component of the electric field (Fig. 7(c)) remains dominant and the strong coupling between the AFM tip and the AgNPs is complemented by a strong coupling between the AgNPs themselves in lateral direction, clearly revealed by the radial component of the electric field in the AgNPs plane (Fig. 7(d)). The maximum lateral field is of $E_{r\_max} = 2.0 \times 10^8$ V/m and its contribution is significant, especially in the plane of AgNPs. The $E_r$–value remains high in the plane of AgNPs ($E_r \approx 5.0 \times 10^7$ V/m), which certainly drives the injected charges in lateral direction to be spread between the AgNPs. This explains the higher maximum and the larger FWHM of the measured surface potential profile in presence of AgNPs (Fig. 6(a)).

A further step in the description of charge trapping and ejection by the AgNPs was to assess the amount of injected charges. The 2D-axisymmetric FEM model was employed, following a previously developed methodology [17], in which the injected charge cloud was represented in lateral direction by a full-Gaussian shape, characterized by a parameter $\sigma_r$, related to the FWHM of the profile ($W_r$) and a half Gaussian shape in-depth in the dielectric/ nanocomposite, characterized by a parameter $\sigma_z$, related to the half of the FWHM ($W_z$) of the in-depth profile. An iterative numerical scheme was applied until the computed surface potential profile was found identical to the measured one. Then the charge density profile was determined and the quantity of injected charges was extracted from the latter. Table 2 summarizes the parameters and the obtained results from the FEM model. The determined from the FEM model $W_r$ for the two structures can be considered as a mirror image of the measured FWHM (W) of the surface potential profile. One can notice the very good agreement between these two parameters for each of the studied structures, without and with AgNPs. The extracted from the FEM model quantities of injected charges for the two structures points to the large capacity of AgNPs to trap charges. Almost twenty times more charges are injected in presence of AgNPs. If one considers here the symmetric behavior of the area under the surface potential profile when applying positive and negative bias for charge injection (Fig. 6(b)), another very important statement can be done: the AgNPs efficiently trap charges regardless their polarity.

Nevertheless, the capability of injection and trapping of charge carriers in the nanocomposite containing AgNPs depends on additional factors, such as size, shape of the AgNPs and distance between them, i.e., their surface density. The distance between the AgNPs is essential for transport processes, mainly tunneling between two AgNPs, whereas the AgNPs-size takes action in the charge injection from the electrode through the electric field intensification. In addition, the injection process is modified according to the size of AgNPs since the work function of nanoparticles differs considerably from that of an infinite metallic plane [66]. The difference accounts for the charging energy of the nanoparticle when an electron is extracted from the latter. Finally, the energy required to remove an electron to infinity from a metal sphere is increased by a factor inversely proportional to the radius of the metal sphere. Thus, the work function gets higher for smaller nanoparticles. Considering the work function for pure silver, which is of $\Phi_{Ag} = 4.64$ eV [40], and applying the expression given by Wood [66], one finds that the work function is increased by 0.05 eV for the large AgNPs, by 0.1 eV for the medium ones, and by 0.15 eV for the small AgNPs, to reach 4.79 eV for the latter. The obtained values for the work function of the AgNPs are reported in Table 1. Besides, the surrounding organosilicon matrix of the AgNPs brings additional complexity in the charge injection and transport processes through the accessibility of charge traps due to their density and their different energy levels.

### D. PROBING THE ENERGETIC PROCESSES WITH AC-ELECTROLUMINESCENCE AT THE ELECTRODE/DIELECTRIC CONTACT IN PRESENCE OF AN AGNPS-PLANE AT THE BOPP INTERFACE

Charge exchange processes at the electrode/dielectric contact are essential for the degradation of insulating polymers (Fig. 8(a)). Under DC stress, charges of the same polarity, in accordance with the applied voltage, can be injected and trapped in the dielectric, and by this limit the field at the electrode and eventually reduce further charge injection, as explained earlier. Under AC stress, charges of both polarities, each one corresponding to the applied half cycle of the voltage, are alternatively injected and trapped near the injecting electrode, then partially extracted during the half cycle under

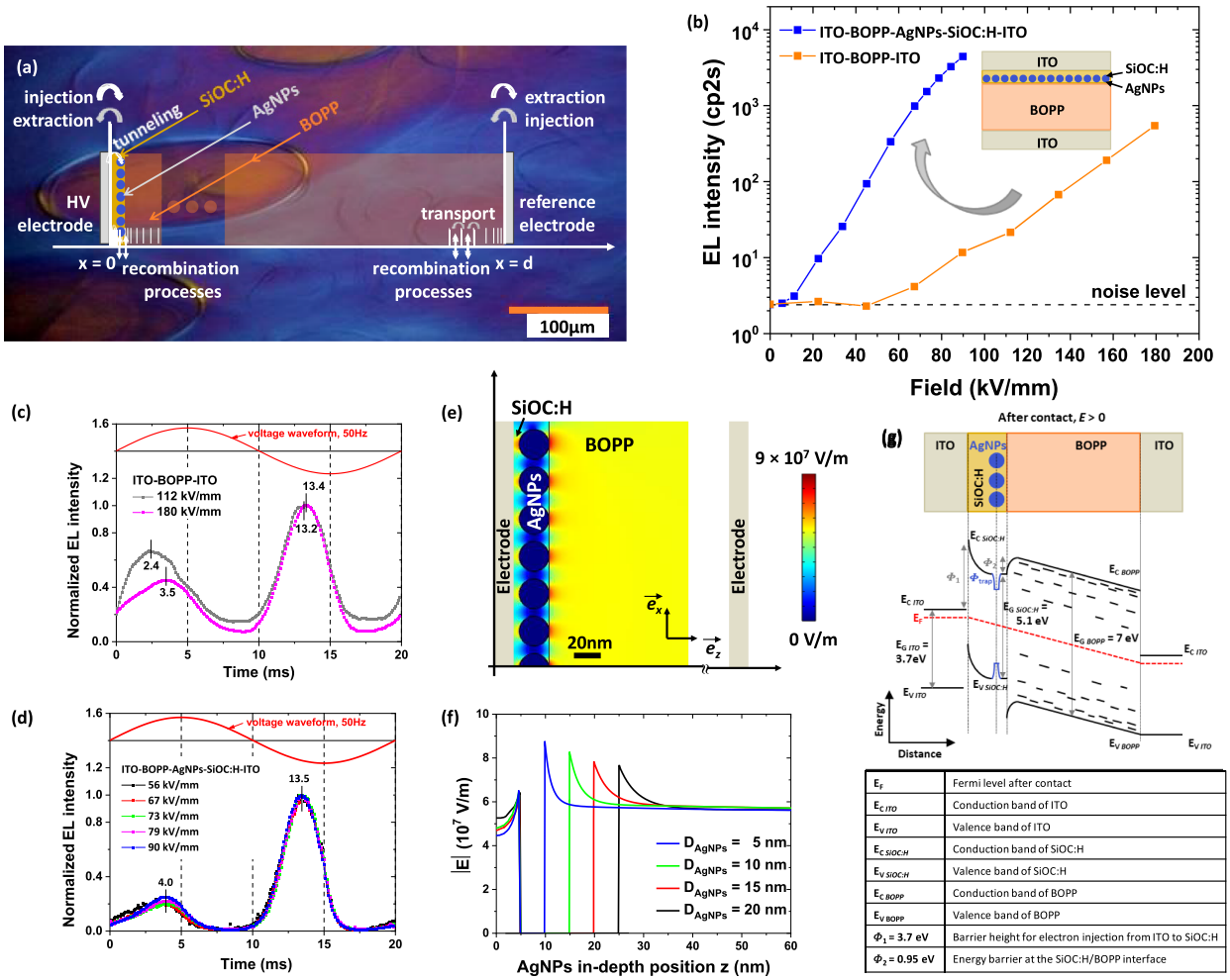


| | |
|---|---|
| $E_F$ | Fermi level after contact |
| $E_{C\,ITO}$ | Conduction band of ITO |
| $E_{V\,ITO}$ | Valence band of ITO |
| $E_{C,SiOC:H}$ | Conduction band of SiOC:H |
| $E_{V\,SiOC:H}$ | Valence band of SiOC:H |
| $E_{C\,BOPP}$ | Conduction band of BOPP |
| $E_{V\,BOPP}$ | Valence band of BOPP |
| $\Phi_1 = 3.7$ eV | Barrier height for electron injection from ITO to SiOC:H |
| $\Phi_2 = 0.95$ eV | Energy barrier at the SiOC:H/BOPP interface |

**FIGURE 8.** **(a) Schematic representations of charge injection and transport processes occurring at the electrode/dielectric interfaces in presence of a AgNPs/SiOC: H stack, (b) electroluminescence vs. electric field (crest values) under 50 Hz AC stress of bare and one side tailored BOPP by a AgNPs/SiOC: H stack. The studied structure involves ITO electrodes, as shown in the inset, (c) phase-resolved EL patterns obtained on bare BOPP, and (d) one side tailored BOPP by an AgNPs/SiOC: H nanocomposite stack. The EL intensity is normalized to the maximum in the second half period of the voltage waveform, (e) spatial distribution of the electric field in the nanocomposite structure after electrostatic calculations in EL configuration, for 1 kV of applied voltage, (f) variation of the electric field around an AgNP in the nanocomposite structure for AgNPs with different sizes, and (g) band diagram of the nanocomposite structure and caption of different symbols. The ITO work function is taken $\Phi_{ITO} = 4.7$ eV [40]. The energy gaps of ITO ($E_{G\,ITO} = 3.7$ eV) and SiOC: H ($E_{G\,SiOC:H} = 5.1$ eV) were determined from the Tauc's plots after spectroscopic ellipsometry measurements of the optical properties of the corresponding layers used in this work. The energy gap of the BOPP ($E_{G\,BOPP} = 7$ eV) was taken from [43]. The electronegativity of SiOC: H and that of BOPP are considered equal, $\chi = 1$ eV.**

opposite polarity. The coexistence of charges of both polarities in a narrow space provides adequate conditions for EL manifestation. This may explain the larger efficiency in light emission under AC stress compared to DC stress. Simulation studies have shown that, in order to account for the EL phase pattern in LDPE under AC stress, a massive charge injection is necessary, providing occurrence of recombination events, essentially within the region of 10 nm from the surface [38]. This behavior points to a probable enhanced ageing near the surface and also to the importance of the boundary conditions in the electrical behavior of insulations [67].

As discussed earlier, a way to probe the energetic processes at the interface consists in detecting the light emitted from the insulating material upon electrical stress application, i.e., to detect the EL of the probed material. This method was initially performed in divergent field configuration and later on implemented for uniform field. Without loss of generality, the main mechanisms leading to EL in dielectrics are as follow:

1) the most straightforward mechanism is direct ionization of the activator centers/traps. On the flip side, it appears to be the less efficient one for dielectrics. To obtain a reasonable EL-yield this mechanism requires a very high electric field strength since the ionization state of the activators lays at about 2 eV above the ground state. In this case the breakdown field of the dielectric would be easily attained and the dielectric destroyed.
2) a second mechanism is excitation of an activator center/trap due to inelastic collisions of highly energetic

electrons, i.e., the so-called hot electrons with it, implying that the kinetic energy of the carriers is directly involved in the EL-process,

3) a third possibility is bipolar charge carrier generation followed by electron-hole recombination, directly involving the potential energy of the carriers. This EL mechanism appears to be highly efficient for dielectrics. It is the one exploited in semiconducting light-emitting devices too.

However, some particularities should be considered when studying EL from insulating polymers like polypropylene and polyethylene. Because the polyolefins are saturated aliphatic polymers, the pure carbon chain C-C or C-H single bonds cannot perform as luminescent centers in the visible domain. Their energy level transitions are high, requiring an energy input of around 8 eV. Accordingly, there is no emission from the repeat unit in polyolefin polymers. If luminescence is detected from these polymers, it is necessarily due to some types of possible chromophore groups in the carbon chain that may arise as a result from electrical degradation. Given the low intensity of the obtained EL-signal in conventional EL-studies, the latter do not allow a convincing interpretation for low applied electric fields. To meet this challenge, an AgNPs/SiOC:H stack was introduced in the system to better control the energetic of charge carriers at the electrode/dielectric (insulating polymer) contact and thus, to amplify the EL-intensity.

EL-intensities of a bare BOPP sample and of the AgNPs/SiOC:H tailored one are shown in Fig. 8(b) as function of the applied electric field. The shape of the obtained EL-field curve for bare BOPP is typical for this sandwich structure ITO-BOPP-ITO. The EL-intensity starts to be distinguishable from the noise level for applied electric fields beyond 50 kV/mm and then exponentially increases with the applied field. Due to the material properties of the ITO electrodes (a highly degenerated n-type semiconductor) the current injection in the BOPP is efficient. In addition, the use of ITO as electrodes in the study, allows to avoid the so-called "red" component in the EL-spectrum under AC stress [27]. The latter is identified as originating from excitation of surface plasmons (SPs) at the electrode/dielectric contact when using metallic electrodes (Au, Ag) and largely documented in the literature for different insulating polymer materials [19], [20], [26], [27]. We will get back to the point of SPs later on in our discussion.

While the bare BOPP sample was studied using electric field strengths up to 180 kV/mm the study of the AgNPs/SiOC:H tailored one was limited to 90 kV/mm with the main reason being the stronger EL intensity. One can clearly notice the very strong enhancement of the EL-signal in presence of AgNPs (Fig. 8(b)). The EL-intensity can be enhanced by more than 2 orders of magnitude for the same applied electric field. Moreover, the detection threshold for EL is much lower for the AgNPs/SiOC:H tailored BOPP sample. Even with an applied field of only 10 kV/mm the BOPP signature becomes readable. The EL-intensity generally scales with the electric field in the material, and more precisely with the number of electrons that are accelerated in the direction of the field, acquiring thus an energy at least equal to the one of the activator center to excite it [68], [69]. The much higher EL-intensity in presence of AgNPs means that the range of energetics of injected charge carriers at the electrode/dielectric contact is extended and the efficiency of the EL-mechanisms is improved.

Complementary information on the underlying processes of this enhanced EL-intensity is achieved through phase-resolved EL-patterns and EL-emission spectra. Fig. 8(c) and (d) compare the EL-phase patterns acquired without and with the AgNPs/SiOC:H nanocomposite stack. Data are obtained at different applied electric fields owing to the large difference in the EL yield (Fig. 8(b)). One can clearly see that there is no strong dependence of the general shape of the EL-phase patterns on the applied electric field. The EL-intensity appears in advance of phase with respect to the applied AC-field. Besides, the EL-phase pattern is steeper compared to the voltage waveform and an asymmetry is observed when changing the polarity of the applied field.

For the bare BOPP sample (Fig. 8(c)), the advance in phase of the EL-phase pattern is more pronounced for lower electric fields, as typically observed for the EL-measurements on insulating polymers [19], [20], [26], [27]. Such EL-phase pattern can be described by charge injection from the electrodes followed by charge recombination in the polymeric insulator. The advance in phase is generally interpreted as a result from polarization of the insulating polymer and the appearance of a space charge field (internal electric field) in the material which depends on the density of carriers and can be added to or subtracted from the applied electric field [69]. For example, starting from zero in the positive half cycle of the applied signal the density of carriers increases with the field due to an increased injection and a stronger release from the traps. Thus, the internal electric field increases with the voltage, inciting a larger density of carriers, their acceleration in the field and action on the excitation of activator centers. The maximum of EL-intensity appears when the injection current is maximum for a given applied electric field. Consequently, the advance in phase appears earlier for lower applied electric fields (Fig. 8(c)). After attaining maximum, the density of available carriers starts to decrease resulting in a lower internal electric field and thus, in a decrease of the EL-yield. The faster loss of charge carriers through recombination determines a steeper decay of the EL-intensity, so one observes a dissymmetry in the phase patterns per half cycle too. Moreover, the EL-phase patterns show the same loss rate of charge carriers per half cycle independently on the intensity of the applied field, suggesting the same loss mechanism.

The advance of phase can be reproduced numerically provided that a substantial field modulation occurs upon charge injection, as performed for a low density polyethylene (LDPE) material [38]. Under a period of 50 Hz of the applied signal, the recombination events are localized within the LDPE material in the 10 – 20 nm region from the electrode/dielectric

contact. Although the radiative charge recombination is considered the main process for EL excitation, different other contributions, like impact excitation by the injected carriers, can be discussed as well, since the EL-peak also scales with the peak of the injection current [38], [70].

For the AgNPs/SiOC:H tailored BOPP sample (Fig. 8(d)) the advance in phase is much less pronounced, almost inexistent, compared to the bare BOPP. In addition, one observes a stabilization of the signal phase in presence of AgNPs, meaning that the advance in phase of the EL-intensity becomes independent from the applied electric field. Such behavior supports our hypothesis that by AgNPs-tailoring one can adjust the energetics of charge carriers at the electrode/dielectric contact. Like for the bare BOPP sample, a dissymmetry of the EL-intensity per half cycle is observed, confirming that the loss mechanism of charge carriers is faster.

An asymmetry in the EL-intensity phase pattern when changing the polarity of the applied signal is observed for both types of samples. This is most likely a consequence of accumulation of the charge carriers close to one of the electrodes, providing in that way a stronger EL-yield during that half cycle of the applied signal. Other factors leading to such asymmetry of the EL-intensity are related to a non-symmetry in the sample configuration, either because of different roughness of both faces like for the studied here BOPP, or, more importantly because of the one-face tailoring by the AgNPs/SiOC:H stack. As can be seen in Figs. 8(c) and (d) the asymmetry of the EL-yield when changing the AC-signal polarity is much more pronounced in presence of AgNPs, providing 5 times stronger EL-intensity for the negative half cycle i.e., when the electrode adjacent to the tailored BOPP face is a cathode.

The much stronger EL-yield of the AgNPs/SiOC:H-tailored BOPP sample can be understood in terms of storing charge carriers in the AgNPs and strongly enhanced internal electric field. Fig. 8(e) shows the electric field distribution in the AgNPs/SiOC:H-tailored BOPP sample for 1 kV of applied potential on the electrode adjacent to the AgNPs-layer, after electrostatic calculations using the FEM model. In the bare BOPP sample (symmetric configuration and homogeneously distributed electric field) such high applied voltage creates an electric field of $|E| = 5.6 \times 10^7$ V/m, or 56 kV/mm, for which the EL-intensity starts to be distinguishable from the noise level in the experiment (Fig. 8(b)). The presence of AgNPs leads to inhomogeneity of the electric field distribution, intensifying the electric field up to $|E| = 7.7 \times 10^7$ V/m on the interface between the AgNPs/SiOC:H stack and the BOPP film. The simulation here is performed with the large AgNPs ($D_{AgNPs} = 20$ nm). The higher electric field would thus promote a stronger charge injection in the BOPP sample and enhance the EL-intensity. The recorded experimental EL-yield is of 2 orders of magnitude higher at this applied voltage (Fig. 8(b)). As demonstrated in the previous section, in presence of AgNPs not only the charge injection is improved (capacitive coupling between the electrode and the AgNPs plane) but also the quantity of trapped charges is strongly enhanced (almost 20 times for the conditions, reported in Table 2). Thus, due to their capability to trap electrical charges and to support hot carrier generation, the AgNPs would regulate the charge injection mechanisms, by playing the role of charge tanks (Coulomb blockage effect). This statement is supported by the experimentally observed stabilization of the EL-phase patterns in presence of AgNPs. Regardless the applied electric field, the advance in phase appears at the same time and the maximum of EL-yield remains identical per half cycle (Fig. 8(d)). The embedding SiOC:H matrix does not bring additional complexity in the system, since its dielectric permittivity is close to the one of BOPP (Section IV.D). Because of its small thickness, it sustains the charge injection from the electrode to the AgNPs through direct tunneling or hopping assisted tunneling, depending on the charge energy, and defines the barrier height at the interface between the AgNPs/SiOC:H stack and the BOPP film.

On the other hand, varying the size of AgNPs permits to vary the electric field at the interface with the polymer, resulting in higher electric field for the smaller in size AgNPs, as can be seen in Fig. 8(f). For example, the electric field at the interface with the BOPP film is enhanced up to $|E| = 8.8 \times 10^7$ V/m, for 1 kV of the applied voltage in presence of very small AgNPs ($D_{AgNPs} = 5$ nm). Thus, the variation in size of the AgNPs allows to adjust the energetics of charge carriers at the electrode/dielectric contact. This also leads to a remarkable conclusion about the experimentally obtained dispersion in size of the AgNPs which, as previously commented (Table 1), is a bit stronger for the large AgNPs ($D_{AgNPs} = 19.7 \pm 4.8$ nm) compared to the one for the medium AgNPs ($D_{AgNPs} = 11.3 \pm 2.4$ nm). Due to their size dispersion, the AgNPs in the plane modulate the electric field, thus ensuring stability in the EL-intensity, since the conformity of the AgNPs-layer to the crater-like patterns surface morphology of the BOPP film, is better (Fig. 3).

The overall physical situation that arises from this nanocomposite structure can be described on the basis of a band diagram (Fig. 8(g)). Data for the different physical properties considered during its construction is given in the table under the band diagram and in the figure caption [43], [71]. Alignment of the Fermi energy level of the different components of the nanocomposite after contact and application of an electric field ($E > 0$, where $E$ is the electric field strength) lead to the following: the electron injection from the ITO electrode to the AgNPs can easily be done via direct tunneling or hopping assisted tunneling through the $\Phi_1$ barrier, given the very small thickness of the SiOC:H layer covering the AgNPs. Then the charge transport from the AgNPs (considered here as artificial charge traps) to the conduction band (CB) of the BOPP, requires a sufficiently high energy to be transferred to the charges in order to escape the charge trap ($E_{trap} = 0.63$ eV for the large AgNPs that create the deepest traps, according to the measurements of the energy gap of the nanocomposites in Section V.B) and to overcome the $\Phi_2$ barrier at the SiOC:H/BOPP interface ($\Phi_2 = 0.95$ eV), which in total gives 1.58 eV. However, after application of an electric field

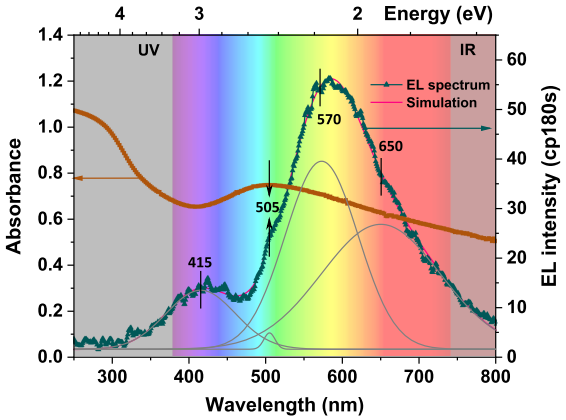


**FIGURE 9. Absorbance and ac-EL spectrum of one face tailored BOPP by an AgNPs/SiOC: H nanocomposite stack. The EL spectrum is obtained with an ac-crest field of 90 kV/mm. The spectrum is deconvoluted into the sum of four Gaussian functions with peak wavelengths indicated in the figure.**

this energetic barrier is reduced. Considering Poole-Frenkel mechanism of the charge transport, due to the high electric field strength and the non-linear electric field behavior around the AgNPs for the applied electric field here (Fig. 8(f)), one estimates this reduction to at least $\beta_{PF}(E)^{1/2} = 0.41$ eV, where $\beta_{PF}$ is the Poole-Frenkel constant and $E$ is the electric field strength, meaning that the electrons can easily flow from the AgNPs/SiOC:H stack to the CB of BOPP. Besides, the energy traps in the BOPP will favor the charge conduction. Given that for smaller in size AgNPs the trap energy is a bit lower, the charge transport will be favored, however corrected for the work function corresponding to the size of the AgNPs (Section V.C, Table 1). All these processes show the complexity of the occurring dielectric charging and transport phenomena and at the same time the narrow link between the electrical degradation of insulating polymers under high electric field, the excitation of EL in insulating polymers, and the EL-yield.

For the above-mentioned reasons, the EL emission spectra of insulating polymers appears extremely appropriate to identify possible activator centers/chemical groups in the material and thus, to describe the relation with the deterioration processes occurring under high electric fields. Fig. 9 presents an EL-spectrum of the AgNPs/SiOC:H tailored BOPP film obtained with an AC-crest field of 90 kV/mm. Approximate readability of the EL-spectrum of the bare BOPP film would require electric fields of at least 180 kV/mm, which is twice higher. As demonstrated in previous studies, the EL-spectrum of bare BOPP, and more generally of polyolefins, can be deconvoluted into different contributions peaking at 415, 505 and 570 nm, with all of these bands being characteristic of existed defects or created chemical functions into the material [19], [20], [26], [27]. For the AgNPs/SiOC:H tailored BOPP sample the same three contributions are present in the EL-spectrum. However, as a difference with the EL-spectrum of bare BOPP (not shown here) a correct description of the EL-spectrum of the tailored BOPP sample requires involvement of a fourth contribution, peaking at 650 nm, i.e., the "red" component (Fig. 9). For the AgNPs/SiOC:H tailored BOPP sample this additional band can be attributed to SPs emission from the AgNPs in SiOC:H environment. As discussed in Section V.B, the SPs are collective excitations of the electron gas and for metals such as gold or silver their relaxation signatures are in the visible range [48], [50], [59]. SPs, as a component of the EL-spectra from insulating polymers, have been reported for BOPP and polyethylene (PE) films. The excitation of these SPs has been identified as originating from the metal electrodes [19], [26]. In the case of Au-electrodes, the "red" component, attributed to the SP-emission, was observed as a broad band at 700-750 nm and being dominant at low AC-field.

It is now generally accepted in the literature that light excitation mechanisms through SPs in MIM structures can be driven by inelastic tunneling of electrons, losing their energy to excite collective oscillations in tunnel junctions [72] and by electrons, that are injected through elastic tunneling and enter the metal as hot carriers [73]. Both modes require surface roughness, since the energy and momentum cannot be simultaneously conserved in a radiative transition without roughness scattering.

Presence of AgNPs in the nanocomposite stack at the electrode/dielectric contact fulfills the conditions for excitation of SPs. The discrete structuring of the metal is an alternative to the surface roughness and appears extremely efficient for excitation of SPs via charge injection/extraction, since under such high electric fields the charges enter the metal nanoparticles with high energies i.e., as hot carriers. The strong SPs excitation is most likely at the origin of the strongly enhanced EL-emission from the BOPP film.

However, the SPs excitation does not constitute the only explanation for the strongly amplified EL-yield. Other possibilities are to be considered too. First, the number of recombination events might be amplified by combining the enhanced charge injection efficiency and the capability of AgNPs to stabilize the injected charges. Second, a sensitization of the BOPP due to the presence of AgNPs may occur, either through the formation of oxidized groups in the AgNPs environment, or through metal enhanced luminescence processes, that involve the LSPR supported by the metallic nanoparticles. This later process, complex indeed, has been recently reported in different nanoscience fields [50], [74], [75], [76]. Another channel for energy transfer from the AgNPs to the BOPP film appears quite efficient. By combination of the EL-emission spectrum with the absorbance one of the AgNPs/SiOC:H-tailored BOPP film (Fig. 9), one can realize the strong coupling at the same energy (2.45 eV or $\lambda = 505$ nm) between the LSPR of the AgNPs and the contribution to the EL-emission spectrum due to recombination-induced luminescence involving conjugated CC bonds bound to CO species [26]. This suggests that AgNPs with different size are sensitive to different chemical groups in the studied polymer, so their response can be tailored. Amplification of the EL-yield based on AgNPs allows to locally input the energy required to excite the activator center, limiting the voltage to be applied in

order to get a readable signal. This limitation actually prevents from electrical breakdown of the studied BOPP film, however allowing to acquire information on the electrical aging of insulating polymers.

## VI. CONCLUSION

This work provides evidence on the possibility to adjust the energetics of charge carriers at the electrode/dielectric contact in insulating polymers (BOPP films) through tailoring by an AgNPs/SiOC:H nanocomposite stack. The applied here approach of combined analyses relies on measurements of the optical properties, the charge injection/storage/ejection and the electroluminescence intensity of these samples. Owing to their reduced size AgNPs allow energy concentration, thus supporting Localized Surface Plasmon Resonances that can be tuned according to the nanoparticle characteristics. The optical response of the tailored BOPP films confirms that depending on their size the AgNPs can be located as artificial deep traps for charges with energy around 0.5 – 0.6 eV. In addition, the capability of AgNPs to store charges is validated at local scale through Kelvin Probe Force Microscopy. The mechanism of charge trapping by AgNPs in the studied configuration resides on the Coulomb blockade effect which solely depends on modification of the electrostatic energy after electron transport to the AgNPs and further trapping. The electrostatic modelling of the electric field distribution in presence of AgNPs provides additional information on the charge injection and transport phenomena at nanoscale. It puts forward the capacitive coupling between the AgNPs and the injecting electrode which ensures a strong local enhancement of the electric field and leads to a heavier charging of the AgNPs, thus confirming the latter as charge tanks. The above results help performing analyses on the origin of the very strong enhancement (more than 2 orders of magnitude) of the electroluminescence intensity recorded from the AgNPs/SiOC:H tailored BOPP films. Not only the light intensity is found much stronger in presence of AgNPs, but the electric field threshold for detection of light emission is strongly decreased.

It is generally admitted that the electroluminescence is a volume effect. However, when excited with an AC-field it comes from the part of the studied film which is in proximity to the injecting electrode. The AgNPs/SiOC:H tailoring of the BOPP film brings additional surface component to the EL-yield. There are indeed different possibilities for the AgNPs contribution to the enhancement of the EL-intensity of the recorded signal:

1) stronger excitation, meaning larger number of recombination events,
2) larger quantum yield due to a larger probability for radiative recombination,
3) energy transfer via the LSPR of AgNPs and
4) radiative surface plasmon relaxation from the AgNPs in organosilicon environment.

They all are based on the energetics of injected charge carriers at the interface between the AgNPs/SiOC:H stack and the polymer. Due to their capability to trap electrical charges and to support hot carrier generation, the AgNPs, as charge tanks, regulate the charge injection mechanisms. This finding is revealed by the experimentally observed stabilization of the EL-phase patterns in presence of AgNPs. Further work will be directed to explore the AgNPs size dependence in the enhanced electroluminescence process in order to probe structural modifications and subsequent electrical aging of polymeric insulating materials.

## ACKNOWLEDGMENT

The authors would like to thank Dr. Christian Laurent from LAPLACE laboratory, Toulouse for fruitful discussions. The authors acknowledge support from the UAR Raymond Castaing of the University of Toulouse and thank Mr Stéphane Le Blond du Plouy for the SEM observations. For the purpose of open access, the authors have applied a CC-BY public copyright license to any Author Accepted Manuscript (AAM) version arising from this submission.

## REFERENCES

[1] L. A. Dissado and J. C. Fothergill, *Electrical Degradation and Breakdown in Polymers* (IEE Materials and Devices Series). London, U.K.: Peter Peregrinus, 1992.

[2] X. Dai, F. Tian, F. Li, S. Zhang, Z. Xing, and J. Wu, "Investigation on charge transport in polypropylene film under high electric field by experiments and simulation," *Energies*, vol. 14, no. 16, Aug. 2021, Art. no. 4722, doi: 10.3390/en14164722.

[3] L. Sanche, "Nanoscopic aspects of electronic aging in dielectrics," *IEEE Trans. Dielectrics Elect. Insul.*, vol. 4, no. 5, pp. 507–543, Oct. 1997, doi: 10.1109/94.625643.

[4] G. Teyssedre and C. Laurent, "Charge transport modeling in insulating polymers: From molecular to macroscopic scale," *IEEE Trans. Dielectrics Elect. Insul.*, vol. 12, no. 5, pp. 857–875, Oct. 2005, doi: 10.1109/TDEI.2005.1522182.

[5] G. Mazzanti, G. C. Montanari, and L. A. Dissado, "Electrical aging and life models: The role of space charge," *IEEE Trans. Dielectrics Elect. Insul.*, vol. 12, no. 5, pp. 876–890, Oct. 2005, doi: 10.1109/TDEI.2005.1522183.

[6] C. Laurent, G. Teyssedre, S. L. Roy, and F. Baudoin, "Charge dynamics and its energetic features in polymeric materials," *IEEE Trans. Dielectrics Elect. Insul.*, vol. 20, no. 2, pp. 357–381, Apr. 2013, doi: 10.1109/TDEI.2013.6508737.

[7] K. C. Kao, "New theory of electrical discharge and breakdown in low-mobility condensed insulators," *J. Appl. Phys.*, vol. 55, no. 3, pp. 752–755, Feb. 1984, doi: 10.1063/1.333133.

[8] V. A. Zakrevskii, N. T. Sudar, A. Zaopo, and Y.. A. Dubitsky, "Mechanism of electrical degradation and breakdown of insulating polymers," *J. Appl. Phys.*, vol. 93, no. 4, pp. 2135–2139, Feb. 2003, doi: 10.1063/1.1531820.

[9] E. Palleau, L. Ressier, Ł. Borowik, and T. Mélin, "Numerical simulations for a quantitative analysis of AFM electrostatic nanopatterning on PMMA by Kelvin force microscopy," *Nanotechnology*, vol. 21, no. 22, Jun. 2010, Art. no. 225706, doi: 10.1088/0957-4484/21/22/225706.

[10] C. Villeneuve-Faure et al., "Kelvin force microscopy characterization of charging effect in thin a-$SiO_xN_y$: H layers deposited in pulsed plasma enhanced chemical vapor deposition process by tuning the silicon-environment," *J. Appl. Phys.*, vol. 113, no. 20, May 2013, Art. no. 204102, doi: 10.1063/1.4805026.

[11] C. Villeneuve-Faure, L. Boudou, K. Makasheva, and G. Teyssedre, "Methodology for extraction of space charge density profiles at nanoscale from Kelvin probe force microscopy measurements," *Nanotechnology*, vol. 28, no. 50, Dec. 2017, Art. no. 505701, doi: 10.1088/1361-6528/aa9839.

[12] C. Villeneuve-Faure, L. Boudou, K. Makasheva, and G. Teyssedre, "Towards 3D charge localization by a method derived from atomic force microscopy: The electrostatic force distance curve," *J. Phys. Appl. Phys.*, vol. 47, no. 45, Nov. 2014, Art. no. 455302, doi: 10.1088/0022-3727/47/45/455302.

[13] D. M. Schaadt, E. T. Yu, S. Sankar, and A. E. Berkowitz, "Charge storage in Co nanoclusters embedded in $SiO_2$ by scanning force microscopy," *Appl. Phys. Lett.*, vol. 74, no. 3, pp. 472–474, Jan. 1999, doi: 10.1063/1.123039.

[14] S.-D. Tzeng and S. Gwo, "Charge trapping properties at silicon nitride/silicon oxide interface studied by variable-temperature electrostatic force microscopy," *J. Appl. Phys.*, vol. 100, no. 2, Jul. 2006, Art. no. 023711, doi: 10.1063/1.2218025.

[15] Z. Z. Lwin et al., "Localized charge trapping and lateral charge diffusion in metal nanocrystal-embedded High-$\kappa$/$SiO_2$ gate stack," *Appl. Phys. Lett.*, vol. 99, no. 22, Nov. 2011, Art. no. 222102, doi: 10.1063/1.3664220.

[16] F. Mortreuil, L. Boudou, K. Makasheva, G. Teyssedre, and C. Villeneuve-Faure, "Influence of dielectric layer thickness on charge injection, accumulation and transport phenomena in thin silicon oxynitride layers: A nanoscale study," *Nanotechnology*, vol. 32, no. 6, Feb. 2021, Art. no. 065706, doi: 10.1088/1361-6528/abc38a.

[17] C. Djaou, C. Villeneuve-Faure, K. Makasheva, L. Boudou, and G. Teyssedre, "Analysis of the charging kinetics in silver nanoparticles-silica nanocomposite dielectrics at different temperatures," *Nano Exp.*, vol. 2, no. 4, Dec. 2021, Art. no. 044001, doi: 10.1088/2632-959X/ac3886.

[18] M. Houssat, C. Villeneuve-Faure, N. L. Dignat, and J.-P. Cambronne, "Nanoscale mechanical and electrical characterization of the interphase in polyimide/silicon nitride nanocomposites," *Nanotechnology*, vol. 32, no. 42, Oct. 2021, Art. no. 425703, doi: 10.1088/1361-6528/ac13ea.

[19] G. Teyssedre, L. Cisse, D. Mary, and C. Laurent, "Identification of the components of the electroluminescence spectrum of PE excited in uniform fields," *IEEE Trans. Dielectrics Elect. Insul.*, vol. 6, no. 1, pp. 11–19, Feb. 1999, doi: 10.1109/94.752004.

[20] G. Teyssedre, G. Tardieu, D. Mary, and C. Laurent, "AC and DC electroluminescence in insulating polymers and implication for electrical ageing," *J. Phys. D: Appl. Phys.*, vol. 34, no. 14, pp. 2220–2229, Jul. 2001, doi: 10.1088/0022-3727/34/14/318.

[21] C. Laurent and G. Teyssedre, "Hot electron and partial-discharge induced ageing of polymers," *Nucl. Instrum. Methods Phys. Res. Sect. B Beam Interact. Mater. At.*, vol. 208, pp. 442–447, Aug. 2003, doi: 10.1016/S0168-583X(03)00649-9.

[22] G.-J. Zhang, K. Yang, M. Dong, W.-B. Zhao, and Z. Yan, "Surface electroluminescence phenomena correlated with trapping parameters of insulating polymers," *Appl. Surf. Sci.*, vol. 254, no. 5, pp. 1450–1455, Dec. 2007, doi: 10.1016/j.apsusc.2007.07.077.

[23] G. Teyssedre and C. Laurent, "Evidence of hot electron-induced chemical degradation in electroluminescence spectra of polyethylene," *J. Appl. Phys.*, vol. 103, no. 4, Feb. 2008, Art. no. 046107, doi: 10.1063/1.2875165.

[24] K. Yang, G.-J. Zhang, D.-M. Tu, and Z. Yan, "Space charge and electroluminescence characteristics of thermally aged LDPE films," *Appl. Surf. Sci.*, vol. 255, no. 5, pp. 2735–2739, Dec. 2008, doi: 10.1016/j.apsusc.2008.08.070.

[25] E. Aubert, G. Teyssedre, C. Laurent, S. Rowe, and S. Robiani, "Electrically active defects in silica-filled epoxy as revealed by light emission analysis," *J. Phys. Appl. Phys.*, vol. 42, no. 16, Aug. 2009, Art. no. 165501, doi: 10.1088/0022-3727/42/16/165501.

[26] B. Qiao, G. Teyssedre, and C. Laurent, "Electroluminescence and cathodoluminescence from polyethylene and polypropylene films: Spectra reconstruction from elementary components and underlying mechanisms," *J. Appl. Phys.*, vol. 119, no. 2, Jan. 2016, Art. no. 024103, doi: 10.1063/1.4939824.

[27] B. Qiao, C. Laurent, and G. Teyssedre, "Evidence of exciton formation in thin polypropylene films under AC and DC fields and relationship to electrical degradation," *IEEJ Trans. Fundam. Mater.*, vol. 136, no. 2, pp. 74–80, 2016, doi: 10.1541/ieejfms.136.74.

[28] M. S. Khalil, "International research and development trends and problems of HVDC cables with polymeric insulation," *IEEE Elect. Insul. Mag.*, vol. 13, no. 6, pp. 35–47, Nov./Dec. 1997, doi: 10.1109/57.637152.

[29] T. L. Hanley, R. P. Burford, R. J. Fleming, and K. W. Barber, "A general review of polymeric insulation for use in HVDC cables," *IEEE Elect. Insul. Mag.*, vol. 19, no. 1, pp. 13–24, Jan./Feb. 2003, doi: 10.1109/MEI.2003.1178104.

[30] G. C. Montanari and P. H. F. Morshuis, "Space charge phenomenology in polymeric insulating materials," *IEEE Trans. Dielectrics Elect. Insul.*, vol. 12, no. 4, pp. 754–767, Aug. 2005, doi: 10.1109/TDEI.2005.1511101.

[31] T. J. Lewis, "Nanometric dielectrics," *IEEE Trans. Dielectrics Elect. Insul.*, vol. 1, no. 5, pp. 812–825, Oct. 1994, doi: 10.1109/94.326653.

[32] M. F. Frechette et al., "Nanodielectrics: A 'universal' panacea for solving all electrical insulation problems?," in *Proc. IEEE 10th Int. Conf. Solid Dielectrics*, 2010, pp. 1–3, doi: 10.1109/ICSD.2010.5568070.

[33] M. Roy, J. K. Nelson, R. K. MacCrone, and L. S. Schadler, "Candidate mechanisms controlling the electrical characteristics of silica/XLPE nanodielectrics," *J. Mater. Sci.*, vol. 42, no. 11, pp. 3789–3799, Jun. 2007, doi: 10.1007/s10853-006-0413-0.

[34] T. Takada, Y. Hayase, Y. Tanaka, and T. Okamoto, "Space charge trapping in electrical potential well caused by permanent and induced dipoles for LDPE/MgO nanocomposite," *IEEE Trans. Dielectrics Elect. Insul.*, vol. 15, no. 1, pp. 152–160, Feb. 2008, doi: 10.1109/T-DEI.2008.4446746.

[35] T. Tanaka et al., "Dielectric properties of XLPE/$Sio_2$ nanocomposites based on CIGRE WG D1.24 cooperative test results," *IEEE Trans. Dielectrics Elect. Insul.*, vol. 18, no. 5, pp. 1482–1517, Oct. 2011, doi: 10.1109/TDEI.2011.6032819.

[36] L. Milliere, K. Makasheva, C. Laurent, B. Despax, L. Boudou, and G. Teyssedre, "Silver nanoparticles as a key feature of a plasma polymer composite layer in mitigation of charge injection into polyethylene under DC stress," *J. Phys. Appl. Phys.*, vol. 49, no. 1, Jan. 2016, Art. no. 015304, doi: 10.1088/0022-3727/49/1/015304.

[37] F. Boufayed et al., "Models of bipolar charge transport in polyethylene," *J. Appl. Phys.*, vol. 100, no. 10, Nov. 2006, Art. no. 104105, doi: 10.1063/1.2375010.

[38] F. Baudoin, D. H. Mills, P. L. Lewin, S. L. Roy, G. Teyssedre, and C. Laurent, "Modeling electroluminescence in insulating polymers under AC stress: Effect of excitation waveform," *J. Phys. Appl. Phys.*, vol. 44, no. 16, Apr. 2011, Art. no. 165402, doi: 10.1088/0022-3727/44/16/165402.

[39] K. Makasheva et al., "Dielectric engineering of nanostructured layers to control the transport of injected charges in thin dielectrics," *IEEE Trans. Nanotechnol.*, vol. 15, no. 6, pp. 839–848, Nov. 2016, doi: 10.1109/TNANO.2016.2553179.

[40] W. M. Haynes Ed., *CRC Handbook of Chemistry and Physics*, Boca Raton, FL, USA: CRC, 2011.

[41] J. Robertson, "High dielectric constant oxides," *Eur. Phys. J. Appl. Phys.*, vol. 28, no. 3, pp. 265–291, Dec. 2004, doi: 10.1051/epjap:2004206.

[42] I. Ciofi, M. R. Baklanov, Z. Tőkei, and G. P. Beyer, "Capacitance measurements and $k$-value extractions of low-$k$ films," *Microelectron. Eng.*, vol. 87, no. 11, pp. 2391–2406, Nov. 2010, doi: 10.1016/j.mee.2010.04.014.

[43] T. D. Huan et al., "Advanced polymeric dielectrics for high energy density applications," *Prog. Mater. Sci.*, vol. 83, pp. 236–269, Oct. 2016, doi: 10.1016/j.pmatsci.2016.05.001.

[44] I. Rytöluoto, A. Gitsas, S. Pasanen, and K. Lahti, "Effect of film structure and morphology on the dielectric breakdown characteristics of cast and biaxially oriented polypropylene films," *Eur. Polym. J.*, vol. 95, pp. 606–624, Oct. 2017, doi: 10.1016/j.eurpolymj.2017.08.051.

[45] M. Raab, V. Hnát, and M. Kudrna, "Fibrillation of polypropylene film as monitored by the sound propagation method," *Polym. Testing*, vol. 6, no. 6, pp. 447–461, 1986, doi: 10.1016/0142-9418(86)90019-X.

[46] L. Guadagno et al., "Dependence of electrical properties of polypropylene isomers on morphology and chain conformation," *J. Phys. Appl. Phys.*, vol. 42, no. 13, Jul. 2009, Art. no. 135405, doi: 10.1088/0022-3727/42/13/135405.

[47] A. Pugliara, C. Bonafos, R. Carles, B. Despax, and K. Makasheva, "Controlled elaboration of large-area plasmonic substrates by plasma process," *Mater. Res. Exp.*, vol. 2, no. 6, Jun. 2015, Art. no. 065005, doi: 10.1088/2053-1591/2/6/065005.

[48] U. Kreibig and M. Vollmer, *Optical Properties of Metal Clusters* (Springer Series in Materials Science). Berlin, Germany: Springer, 1995.

[49] H. Baida et al., "Quantitative determination of the size dependence of surface plasmon resonance damping in single Ag@$SiO_2$ nanoparticles," *Nano Lett.*, vol. 9, no. 10, pp. 3463–3469, Oct. 2009, doi: 10.1021/nl901672b.

[50] A. Scarangella et al., "Detection of the conformational changes of *Discosoma* red fluorescent proteins adhered on silver nanoparticles-based nanocomposites via surface-enhanced Raman scattering," *Nanotechnology*, vol. 30, no. 16, Apr. 2019, Art. no. 165101, doi: 10.1088/1361-6528/aaff79.

[51] D. E. Aspnes, "Plasmonics and effective-medium theories," *Thin Solid Films*, vol. 519, no. 9, pp. 2571–2574, Feb. 2011, doi: 10.1016/j.tsf.2010.12.081.

[52] A. Pugliara, M. Bayle, C. Bonafos, R. Carles, M. Respaud, and K. Makasheva, "Predictive modelling of the dielectric response of plasmonic substrates: Application to the interpretation of ellipsometric spectra," *Mater. Res. Exp.*, vol. 5, no. 3, Mar. 2018, Art. no. 035027, doi: 10.1088/2053-1591/aab32b.

[53] P. Makuła, M. Pacia, and W. Macyk, "How to correctly determine the band gap energy of modified semiconductor photocatalysts based on UV–Vis spectra," *J. Phys. Chem. Lett.*, vol. 9, no. 23, pp. 6814–6817, Dec. 2018, doi: 10.1021/acs.jpclett.8b02892.

[54] R. Carles et al., "Plasmon-resonant Raman spectroscopy in metallic nanoparticles: Surface-enhanced scattering by electronic excitations," *Phys. Rev. B*, vol. 92, no. 17, Nov. 2015, Art. no. 174302, doi: 10.1103/PhysRevB.92.174302.

[55] A. N. Koya and J. Lin, "Charge transfer plasmons: Recent theoretical and experimental developments," *Appl. Phys. Rev.*, vol. 4, no. 2, Jun. 2017, Art. no. 021104, doi: 10.1063/1.4982890.

[56] S. Linic, S. Chavez, and R. Elias, "Flow and extraction of energy and charge carriers in hybrid plasmonic nanostructures," *Nature Mater.*, vol. 20, no. 7, pp. 916–924, Jul. 2021, doi: 10.1038/s41563-020-00858-4.

[57] V. K. Sangwan and M. C. Hersam, "Neuromorphic nanoelectronic materials," *Nature Nanotechnol.*, vol. 15, no. 7, pp. 517–528, Jul. 2020, doi: 10.1038/s41565-020-0647-z.

[58] M. Mirigliano et al., "A binary classifier based on a reconfigurable dense network of metallic nanojunctions," *Neuromorphic Comput. Eng.*, vol. 1, no. 2, Dec. 2021, Art. no. 024007, doi: 10.1088/2634-4386/ac29c9.

[59] G. Cacciato et al., "Enhancing carrier generation in $TiO_2$ by a synergistic effect between plasmon resonance in Ag nanoparticles and optical interference," *Nanoscale*, vol. 7, no. 32, pp. 13468–13476, 2015, doi: 10.1039/C5NR02406D.

[60] P. A. Bolla, S. Huggias, M. A. Serradell, J. F. Ruggera, and M. L. Casella, "Synthesis and catalytic application of silver nanoparticles supported on *Lactobacillus kefiri* S-layer proteins," *Nanomaterials*, vol. 10, no. 11, Nov. 2020, Art. no. 2322, doi: 10.3390/nano10112322.

[61] A. Manjavacas, J. G. Liu, V. Kulkarni, and P. Nordlander, "Plasmon-induced hot carriers in metallic nanoparticles," *ACS Nano*, vol. 8, no. 8, pp. 7630–7638, Aug. 2014, doi: 10.1021/nn502445f.

[62] X. Wang et al., "Enhancement of radiative plasmon decay by hot electron tunneling," *ACS Nano*, vol. 9, no. 8, pp. 8176–8183, Aug. 2015, doi: 10.1021/acsnano.5b02361.

[63] M. L. Brongersma, N. J. Halas, and P. Nordlander, "Plasmon-induced hot carrier science and technology," *Nature Nanotechnol.*, vol. 10, no. 1, pp. 25–34, Jan. 2015, doi: 10.1038/nnano.2014.311.

[64] K.-C. Kao and W. Hwang, *Electrical Transport in Solids: With Particular Reference to Organic Semiconductors*. New York, NY, USA: Pergamon Press, 1981.

[65] C. Rigoudy, K. Makasheva, M. Belhaj, S. Dadouch, G. Teyssedre, and L. Boudou, "Rational engineering of the dielectric properties of thin silica layers with a single plane of AgNPs," in *Proc. IEEE 3rd Int. Conf. Dielectrics*, 2020, pp. 205–208, doi: 10.1109/ICD46958.2020.9341862.

[66] D. M. Wood, "Classical size dependence of the work function of small metallic spheres," *Phys. Rev. Lett.*, vol. 46, no. 11, pp. 749–749, Mar. 1981, doi: 10.1103/PhysRevLett.46.749.

[67] T. Christen, "HVDC insulation boundary conditions for modeling and simulation," *IEEE Trans. Dielectrics Elect. Insul.*, vol. 22, no. 1, pp. 35–44, Feb. 2015, doi: 10.1109/TDEI.2014.004559.

[68] D. Curie, "Sur le mécanisme de l'électroluminescence. I. Considérations théoriques," *J. Phys. Radium*, vol. 14, no. 10, pp. 510–524, 1953, doi: 10.1051/jphysrad:019530014010051000.

[69] D. Curie, "Sur le mécanisme de l'électroluminescence, - II. Applications aux faits expérimentaux," *J. Phys. Radium*, vol. 14, no. 12, pp. 672–686, 1953, doi: 10.1051/jphysrad:019530014012067200.

[70] H. R. Zeller, "Noninsulating properties of insulating materials," in *Proc. Annu. Rep.. Conf. Elect. Insul. Dielectric Phenomena*, 1991, pp. 19–47, doi: 10.1109/CEIDP.1991.763333.

[71] Y. Park, V. Choong, Y. Gao, B. R. Hsieh, and C. W. Tang, "Work function of indium tin oxide transparent conductor measured by photoelectron spectroscopy," *Appl. Phys. Lett.*, vol. 68, no. 19, pp. 2699–2701, May 1996, doi: 10.1063/1.116313.

[72] J. R. Kirtley, T. N. Theis, J. C. Tsang, and D. J. DiMaria, "Hot-electron picture of light emission from tunnel junctions," *Phys. Rev. B*, vol. 27, no. 8, pp. 4601–4611, Apr. 1983, doi: 10.1103/PhysRevB.27.4601.

[73] P. Canet, C. Laurent, J. Akinnifesi, and B. Despax, "Light emission from metal-insulator-metal structures," *J. Appl. Phys.*, vol. 73, no. 1, pp. 384–393, Jan. 1993, doi: 10.1063/1.353861.

[74] R. H. Friend et al., "Electroluminescence in conjugated polymers," *Nature*, vol. 397, no. 6715, pp. 121–128, Jan. 1999, doi: 10.1038/16393.

[75] A. Barbieri, G. Accorsi, and N. Armaroli, "Luminescent complexes beyond the platinum group: The d10 avenue," *Chem. Commun.*, no. 19, pp. 2185–2193, 2008, doi: 10.1039/b716650h.

[76] Z. Cheng, G. Li, and M. Liu, "Metal-enhanced fluorescence effect of Ag and Au nanoparticles modified with rhodamine derivative in detecting Hg2+," *Sensors Actuators B Chem.*, vol. 212, pp. 495–504, Jun. 2015, doi: 10.1016/j.snb.2015.02.050.